IISc Theses Abstracts

Contents

IISc THESES ABSTRACTS

Thesis Abstract (Ph. D.)
Identification and characterization of meiotic DNA repair sites of rat pachytene by
Lakshmi Ramachandra
Research supervisor: M. R. S. Rao
Department: Biochemistry

1. Introduction

Meiosis is a unique developmental stage in the life cycle of all sexually reproducing eukaryotes. In higher eukaryotic species, the meiotic division occurs during gametogenesis. The meiotic cell cycle is of fundamental importance as it gives rise to genetic diversity in population. This variation arises as a result of genetic recombination at the pachytene interval and the independent assortment of nonhomologous chromosomes.

In addition to the events of recombination at the pachytene interval of meiosis, high levels of DNA repair synthesis have also been documented in diverse systems as lilium and mouse meiocytes[1]. Correspondingly, an increase in the levels of β polymerase, the main repair enzyme, during this interval has also been noted in several organisms[2–4]. Although the DNA repair synthesis is believed to be a consequence of the events of recombination, evidence remains circumstantial[1]. The present investigation was initiated to further our understanding of the role of DNA repair synthesis at the pachytene interval of the meiotic prophase in rat spermatocytes.

2. Experimental and discussion

As an initial step in this investigation, the centrifugal elutriation technique was standardised for the isolation of rat pachytene spermatocytes. Due to the presence of contaminating replicating spermatocytes and post-meiotic spermatids in the preparations, it was necessary to optimise the conditions to specifically measure only the DNA repair activity of pachytene spermatocytes. Therefore, the repair activity was monitored in the presence of aphidicolin, an inhibitor of replicative DNA synthesis. Since incorporation was aphidicolin insensitive and localised to the pachytene nuclei it is likely to be catalysed by DNA polymerase β, the main repair enzyme.

A novel methodology for the isolation of the meiotic DNA repair sites was developed by combining two independent techniques: (a) Incorporation of bromodeoxyuridine (BrdUrd) into the repair sites of rat pachytene spermatocytes in the presence of aphidicolin followed by the release of the repair sites as ssDNA fragments by mild akali. (b) Isolation of BrdUrd-containing ssDNA fragments with the aid of anti-BrdUrd antibodies. Polyclonal antibodies against BrdUrd were therefore raised in rabbits.

The meiotic DNA repair sites were found to constitute approximately 1.75% of the total rat pachytene genome. The alkali-released repair sites constituted 40% of the total repair sites. These sites which were released as nucleoprotein complexes consisted of two DNA size classes: a dominant size class of 4–7 S and a small size class of 9–12 S. Despite carrying out the incorporation in the presence of aphidicolin, several control experiments were carried out to conclusively show that the meiotic DNA repair sites isolated were clearly distinct from Okazaki fragments and other replicative intermediates.

Southern hybridization of the repair sites to restriction enzyme-digested DNA was carried out. Though the repair sites were found throughout the genome, strong signals corresponding to the various DNA families were observed. The 1.3- and 2.4-kbp *EcoRI* repeat family to which the repair DNA hybridized were gel purified and cloned. Individual repair positive and negative clones were then identified by hybridization with meiotic repair sites. A repair positive (1.3A) and a repair negative (1.3B) clone were sequenced.

The repair positive (1.3A) clone was found to contain (a) a $(CA)_{22}$ repeat, (b) a $(CAGA)_6$ repeat, and (c) four sequences sharing a high percentage of homology to the various reported HVMS sequences. One of the HVMS-like sequences, 5'GGGAGGGAGTGAGGATTC 3' was found to detect polymorphism in humans. Another of the HVMS-like sequences, 5' AGACTGAG GCAGGTAGCAAGG 3' was found to contain a 5' GGCAGG 3' motif, shown to be responsible for the germline instability of HVMS sequences in mouse[5].

The repair negative clone was found to contain (a) a $(CA)_6$ repeat, and (b) an HVMS-like sequence. This sequence, however, did not contain a 5' GGCAGG 3' motif.

Of the 20 1.3- and 2.4-kbp clones selected, only two of the repair positive clones (apart from the 1.3A clone) were found to contain a $(CA)_n$ stretch of 12 repeats. None of the clones, either repair positive or negative, apart from the 1.3A clone, were found to contain a $(CAGA)_6$ repeat. The presence of the $(CAGA)_6$ and $(CA)_{22}$ repeat in the 1.3A clone could therefore be fortuitous or alternatively, not identified, since specific fragment lengths of DNA have been used in the investigation.

The presence of the 5' GGCAGG 3' sequence within one of the HVMS-like sequences in the repair positive clone represents a striking difference between the 1.3A (repair positive) and the 1.3B (repair negative) clones. One could therefore postulate that the repair synthesis during the pachytene interval is a consequence of the events leading to the germline propagation of HVMS sequences. However, further evidence is required to substantiate this postulate.

Reference

1. STERN, H. AND HOTTA, Y.   *Meiosis* (Moen, P. B., ed.), pp. 303–329, 1987, Academic Press.

2. NOWAK, R., WOSZCZYNSKI, M. AND   *Expl Cell Res.*, 1980, **191**, 51–56.
   SIEDLECKI, J. A.

3. GRIPPO, P., GEREMIA, R.,   *Cell Differentiation*, 1987, **7**, 237–248.
   LOCOROTONDO, G. AND MONESI, V

4. SAKAGUCHI, K. AND LU, B. C.   *Mol. Cell. Biol.*, 1982, **2**, 752–757

5. MITANI, K., TAKAHASHI, Y. AND   *J Biol. Chem.*, 1990, **265**, 15203–15210.
   KOMINAMI, R.

Thesis Abstract (Ph.D.)
Studies in heterocycles. a) Synthesis of oxygen and nitrogen polycyclic aromatic compounds *via* o-quinone methides, and b) Photoisomerization of spironaphthalenones by Ashis Baran Mandal
Research supervisor: T. R. Kasturi
Department: Organic Chemistry

1. Introduction

o-Benzoquinone methides **1** and 1,2-naphthoquinone-1-methides **2** are reactive unstable interme-diates involved in the chemistry of phenols and naphthols[1-3]. Since these intermediates are α, β-unsaturated carbonyl compounds, they add neucleophiles to the methide carbon or undergo po-lymerization in the absence of suitable additional dienophiles or react with dienophiles in Diels–Alder fashion to give chromans[4-6]. Kasturi *et al*[7]. have reported a new method for the generation of 1,2-naphthoquinone-1-methide from 1-bromomethyl-2-(2'-tetrahydropyranyloxy)naphthalene **3a** under mild basic condition and subsequent synthesis of polycyclic aromatic compounds **4a** and **5a** in the presence of tetrachlorocatechol (TCC) in acetone. With a view to generalise this reaction with different substrates **3b–c** and also to extend this methodology to phenol and quinol systems, the reaction was carried out with bromomethyl phenols/quinol **10a–d** and **3d**. The results ob-tained in this effort are discussed below.
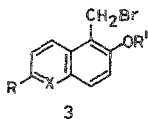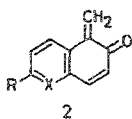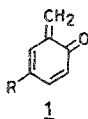
2. Results and discussion

Reaction of 6-*tert*-butyl-1-bromomethyl-2-(2'-tetrahydropyranyloxy)naphthalene **3b** with TCC in the presence of anhydrous K_2CO_3 in acetone gave pyranopyran **6b**, 1,2-naphthoquinone-1-methide dimers **7b** and **8b** and two diastereomeric compounds **4b** and **5b**. A mechanism invoking the base-induced cleavage of the pyranyl ether **3b** to 1,2-naphthoquinone-1-methide **2b** as the first step has been postulated. 1,2-Naphthoquinone-1-methide **2b**, thus generated, gives the dimers **7b** and **8b** and also undergoes Michael addition with TCC followed by the elimination of chloride to give a diketone intermediate **9**, which further undergoes aldolisation with acetone to give diastereomers **4b** and **5b**[8]. The last step of the postulated mechanism, *viz.*, aldolisation has been demonstrated using unsymmetrical keton(ethyl methyl keton) when the corresponding diastereomeric compounds **4c, 5c** and **5d** were isolated. The structure of the diastereomeric com-pounds was assigned based on spectral data. A similar reaction of the bromides **3b–c** with tetra-bromocatechol in acetone gave the diastereomeric compounds **4d–e** and **5e–f** along with other products.

The reaction of bromide **10a** with TCC in K_2CO_3 in acetone resulted in the formation of diastereomeric products **11a** and **12a**, along with TCC ethers **13a** and **14a**. Formation of diastereomeric products **13a** and **14a** is indicative of the generation of *o*-benzoquinone methide **1a** under the reaction conditions. A suitable mechanism for the formation of TCC ethers has been proposed[9]. The reaction has been generalised by the reaction of bromides **10b–c** with TCC/TBC in acetone/ethyl methyl ketone when similar compounds **11b–e**, **12b–f**, **13b–d** and **14b–d** were obtained.

The *in-situ* generation of 5,6-quinolinedione-5-methide **2d** and 6-methylene-4 (2'-pyridyl)-cyclohexa-2, 4-diene-1-one **1d** from 5-bromomethyl-6-acetoxyquinoline **3d** and (4(2'-pyridyl)-2-bromomethyl phenylacetate **10d** and subsequent reaction with TCC in acetone in K_2CO_3 gave spirocyclic nitrogen polyaromatic compounds.

Oxidation of 2-naphthols with *o*-bromanil has been reported to give α- and β-spironaph-thalenones[10]. Similarly, several spironaphthalenones **15a–g** and **16a–g** have been synthesised by the reaction of 2-naphthols with *o*-bromanil. Photoisomerization of these spironaphthalenones involving a β-C–O bond cleavage has been studied in detail and this threw some light on the electronic factors involved in the novel rearrangement. A mechanism involved in the intermediacy of spirocyclohexadienone **17** formed by the initial β-C–O bond cleavage of the spironaphthale-nones has been proposed for the above photoisomerization[11].

1   **2**   **3**

a: R = H, R¹ = THP, X = CH ;   b: R = ᵗBu, R¹ = THP, X = CH

c: R = Br, R¹ = THP, X = CH ;   d: R = H , R¹ = COCH₃ , X = N

4
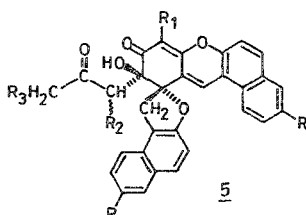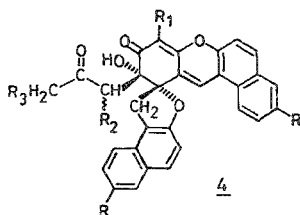
a: R = R₂ = R₃ = H, R₁ = Cl

b: R = ᵗBu, R₁ = Cl , R₂ = R₃ = H

c: R = ᵗBu, R₁ = Cl , R₂ = H, R₃ = CH₃

d: R = ᵗBu, R₁ = Br , R₂ = R₃ = H

e: R = R₁ = Br , R₂ = R₃ = H

5

a: R = R₂ = R₃ = H , R₁ = Cl

b: R = ᵗBu, R₁ = Cl , R₂ = R₃ = H

c: R = ᵗBu, R₁ = Cl , R₂ = βCH₃ , R₃ = H

d: R = ᵗBu, R₁ = Cl , R₂ = H, R₃ = CH₃

e: R = ᵗBu, R₁ = Br , R₂ = R₃ = H

f: R = R₁ = Br , R₂ = R₃ = H
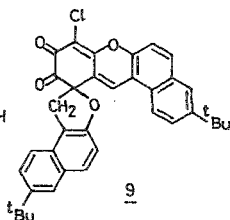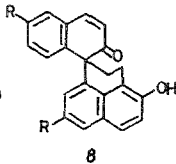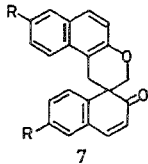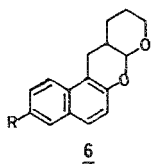
6   **7**   **8**   **9**

10

a: R = H , R¹ = THP ; b: R = Cl , R¹ = THP

c: R = Br, R¹ = THP ; d: R = Py , R¹ = COCH₃

Structures 11 and 12
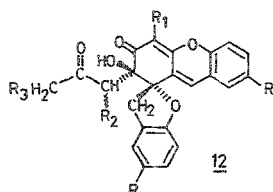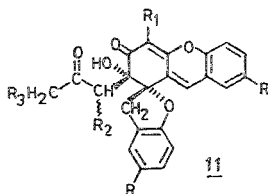
a: R = R$_2$ = R$_3$ = H , R$_1$ = Cl
b: R = R$_1$ = Cl , R$_2$ = R$_3$ = H
c: R = Br, R$_1$ = Cl , R$_2$ = R$_3$ = H
d: R = Br, R$_1$ = Cl, R$_2$ = H , R$_3$ = CH$_3$
e: R = R$_2$ = R$_3$ = H , R$_1$ = Br

a: R = R$_2$ = R$_3$ = H , R$_1$ = Cl
b: R = R$_1$ = Cl, R$_2$ = R$_3$ = H
c: R = Br, R$_1$ = Cl, R$_2$ = R$_3$ = H
d: R = Br, R$_1$ = Cl, R$_2$ = βCH$_3$, R$_3$ = H
e: R = Br, R$_1$ = Cl, R$_2$ = H , R$_3$ = CH$_3$
f: R = R$_2$ = R$_3$ = H , R$_1$ = Br

Structures 13 and 14
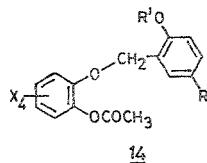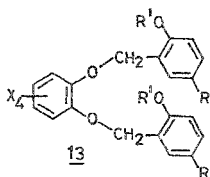
a: R = H , R^1 = THP , X = Cl ; b: R = X = Cl , R^1 = THP
c: R = Br, R^1 = THP, X = Cl ; d: R = H , R^1 = THP , X = Br

Structures 15, 16 and 17
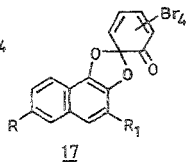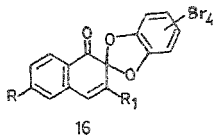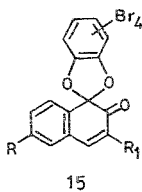
a: R = R$_1$ = H ; b: R = ^{t}Bu, R$_1$ = H ; c: R = cyclohexyl , R$_1$ = H
d: R = H , R$_1$ = CH$_3$; e: R = CN , R$_1$ = H ; R = OCH$_3$, R$_1$ = H
g: R = Br , R$_1$ = H

References

1. DESIMONI, C. AND TACCONI, G.   *Chem. Rev*, 1975, **75**, 651–692.

2. TALLY, J. J.   *J. Org. Chem.*, 1985, **50**, 1695–1699.

3. CHOUHAN, M. S., DEAN, F. M.,   *J. Chem. Soc Perkin I*, 1973, 120–125.
   MATKIN, D. AND ROBINSON, M. L.

4. BOLON, D. A.   *J. Org. Chem.*, 1970, **35**, 3666–3670.

5. ARDUINI, A., BOSI, A., POCHINI, A.   *Tetrahedron*, 1985, **41**, 3095–3103.
   AND UNGARO, R.

6 INOUE, T., INOUE, S. AND SATO, K.   *Bull. Chem Soc. Jap.*, 1990, **63**, 1647–1652.

7. KASTURI, T. R. *et al.*   *Indian J. Chem. B.*, 1986, **25**, 1091–1092.

8. KASTURI, T. R. *et al.*   *Tetrahedron*, 1991, **47**, 5245–5258.

9. KASTURI, T. R. *et al.*   *Tetrahedron*, 1993, **49**, 2751–2760.

10. KASTURI, T. R., ARUNACHALAM, T.   *J. Chem. Soc. (C)*, 1970, 1257–1259.
    AND SUBRAMANYAM, G.

11. KASTURI, T. R., MANDAL, A. B.,   *Tetrahedron*, 1992, **48**, 8841–8848.
    GANESH PRASAD, K. B. AND RAJU, G. J.

Thesis Abstract (Ph. D.)
Analysis of the characteristics of an SF_6 rotating arc by a mathematical model by K. P. Guruprasad
Research supervisors: M. S. Naidu and M. Ramamoorty (CPRI)
Department: High Voltage Engineering

1. Introduction

There have been many investigations on the SF_6 gas blast arcs which find application in HV and EHV circuit breakers. However, there are only a few investigations on rotating arcs which have found wide-ranging applications in medium-voltage switchgear and arc heaters. Significant among the rotating arc studies are the investigations of Spencer[1], Kopainsky and Schade[2] and Kolacinski *et al*[3]. In the study of Spencer, detailed work on SF_6 arc rotating in an annular gap between a rod electrode and metallic cylinder has been reported. This type of contact arrangement is one of the systems used in SF_6 rotating arc circuit breakers, the other being ring electrode arrangement. Characteristics of the rotating arc with respect to the effect of different arc currents, magnitude of the flux density and phase difference have been discussed by him. The arc has been considered to have a uniform cross section.

2. Contribution of the thesis

In the present work, a fluid dynamic arc model has been developed for an SF_6 rotating arc between two ring electrodes. This incorporates the following improvements over the previous work:

(i) No *a priori* assumption has been made regarding the radial temperature distribution of the arc.

(ii) Spatial variation of plasma properties has been considered which is consistent with the radial variation of the temperature of the arc.

(iii) The variation of drag coefficient over the arcing period has been taken into account which resulted in better estimation of the convective heat transfer from the arc.

Digital simulation of the arc characteristics was carried out to study the temporal variations of (i) arc velocity, (ii) arc core temperature, (iii) electrical conductivity, (iv) arc voltage, (v) electric field, and (vi) temperature profiles. It has been possible to incorporate the radial variation of arc properties because of the finite-difference technique adopted for the formulation and solution of the energy balance equations.

Arc characteristics have been obtained for the following three cases:

Case 1: A three-zone arc model has been considered and the three zones are: (a) the electrically conducting arc core, (b) the transition region called the thermal boundary layer, and (c) the bulk SF_6 gas. The volume of SF_6 gas is considered to be so large that its temperature remains at the ambient value irrespective of the variations in the temperature of the arc. Here, two arc currents, 1.4 and 4.2 kA peak, have been studied for a 10 mS arcing period[4].

Case 2: A finite volume of SF_6 gas is considered and the effect of two different volumes of SF_6 gas on the arc temperature has been investigated[5]. The interrupter volumes considered are 0.003 and 0.006 m^3. Since one of the important design parameters for a circuit breaker is the size of the interrupter this investigation has a practical significance. So far, there has not been any investigation which correlates the characteristics of a rotating arc with interrupter volume.

Case 3: The choice of magnetic flux density in the design of rotating arc interrupters needs no emphasis as it is obvious that the rotating arc characteristics depend on the magnetic field responsible for the arc movement. In the present work, the range of flux density in which there is a strong influence of the magnetic field on the arc characteristics has been established for the interrupter volume studied. The range of flux density studied is from 25 to 100 mT/kA for an interrupter volume of 0.003 m^3.

A comparison was made of some of the results obtained in the present work, such as the variation of core temperature, current density and area of the arc with time, with the earlier results of Spencer. Both the sets of results show good agreement as far as the trends of these arc characteristics are concerned. However, the other results like temperature profiles and volume effect on the arc characteristics could not be compared with any other previous work, as similar results, either experimental or theoretical, have not appeared in literature.

From the present study, it has been possible to arrive at the temperature profiles of rotating arcs which prove that it is incorrect to assume uniform temperature throughout the arc cross section. More accurate determination of current distribution enables a better estimation of arc voltage. The effect of two important design parameters, *viz.*, volume of the interrupter and the magnetic field have been investigated. For the first time, it has been shown that the efficacy of arc rotation cannot be enhanced indefinitely by increasing the magnetic flux density with a finite volume of SF_6 gas in an interrupter. Also, volume effect on electrical conductivity and temperature of the arc has been clearly established.

References

1. SPENCER, J. W.   *Some investigations of the behaviour of a rotating arc discharge*, Ph. D. Thesis, University of Liverpool, 1987.

2. KOPAINSKY, J. AND SCHADE, E.   Investigations of a rotating magnetically driven SF₆ arc, *IEEE Conf on Gas Discharges*, pp. 83–85, 1976

3. KOLACINSKI, Z., CAMPBELL, L. C. AND ZDANOWICZ, L. S.   Spiral arc quenching, *IEEE Trans.*, 1992, PD-7, 822–828.

4. GURUPRASAD, K. P., SARMA, C. S., RAMAMOORTY, M. AND NAIDU, M. S.   Investigation of the characteristics of an SF₆ rotating arc by a mathematical model, *IEEE Trans.*, 1992, PD-7, 727–733.

5. GURUPRASAD, K. P, SARMA, C. S., RAMAMOORTY, M. AND NAIDU, M. S.   Digital simulation of an SF₆ rotating arc discharge, *Proc X Int. Conf on Gas Discharges and Applications*, Vol. 1, Swansea, UK, 1992.

Thesis Abstract (Ph. D.)
Field soil moisture regimes and hydrology of irrigated plots by Lakshman Nandagiri
Research supervisor: Rama Prasad
Department: Civil Engineering

1. Introduction

Conjunctive use of available surface and groundwater resources requires a knowledge of the manner and rates at which these sources are replenished by natural precipitation. Since hydrological flow paths cannot be uniquely identified from catchment or regional scale observations, the present investigation was undertaken to study the hydrological responses and water-flow paths within irrigated cropped field plots.

2. Methodology

The site of the field study was an irrigated farmland located close to Bangalore, India. The experimental programme involved measurements of soil, crop and meteorological data, and the field water balance components for the period May 1991–May 1992. Daily rainfall was measured with a standard nonrecording gauge and irrigation application from a groundwater source was measured using a calibrated water meter. For a part of the study, surface runoff from rainfall was measured by routing it through a collecting tank fitted with a water meter. Two observation wells were used to monitor the position of the groundwater table. While depth-wise soil matric potentials were measured at not less than weekly intervals using tensiometers, profile soil moisture was concurrently measured using a Wallingford neutron probe. Brass or stainless steel neutron access tubes were sunk to depths varying between 0.6 and 1.9 m in four field plots, which during the course of the study were planted to various crops including finger millets, mulberry, tomato, ladies finger, sunflower and chilli. A Class A pan was installed in the field and daily pan evaporation recorded. This was supplemented with other meteorological data obtained from a climatological station located close to the experimental site. Field soil samples were used to determine bulk density, particle size distribution, particle density, organic matter content and laboratory desorption characteristics. Plant factors of leaf area index and crop height were also periodically measured.

3. Results and discussion

Overall results of the present study indicate the feasibility of examining the hydrological responses of the crop root-zone based on weekly water balance computations. While recognising the

complex nature of interactions in the soil–plant–atmosphere continuum, the study has shown that several of the hydrologic processes can still be successfully modelled using easily available input data.

3.1. *Atmospheric processes*

Analysis of daily rainfall data indicated the existence of distinct wet and dry seasons during a year and the presence or absence of a few large rainfall events determined the magnitude of the annual total.

A comprehensive literature review has been used to highlight the attempts made to model the important ET process from meteorological data. The Doorenbos and Pruitt methodology[1] for estimating reference crop ET by several methods has been replaced with a simple algorithm that eliminates the use of cumbersome graphs and tables. Using the pan evaporation method as reference, the Penman and Priestley–Taylor models have been evaluated under existing conditions. A new, simple method of estimating the existing crop cover has been presented in which the need for laborious leaf area index measurements is eliminated.

3.2. *Soil processes*

An evaluation of several available texture-based models for the soil moisture characteristic (SMC) highlighted the fact that their performances as estimators of the *in-situ* and laboratory-measured SMCs were determined by the nature of their underlying data set. A simple log–log adaptation of a model developed from a data set consisting of field-measured retention was the best estimator of the *in-situ*-measured SMC of not only the sandy loam soil of the present study but also of a loamy sand taken from literature. While pointing out the superiority of the van Genuchten's SMC model[2], estimation of its parameters from known parameters of the Brooks and Corey model[3] has been proposed. Also, the van Genuchten model for the unsaturated hydraulic conductivity [$K(\theta)$] was found to yield estimates closer to field-measured ones, in comparison to Campbell's model[4].

3.3. *Field water balance*

Weekly water balance components during wet (Fig. 1) and dry seasons were computed in two plots under differing land-use conditions. During the wet season, surface runoff from monsoon
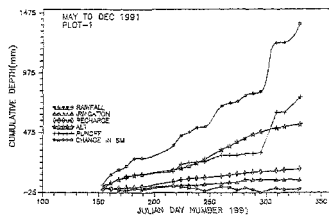
FIG. 1. Cumulative field water balance components in plot-1 during the wet season of 1991.
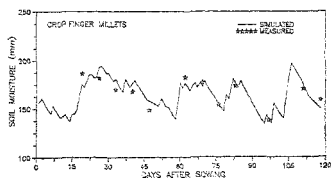
FIG. 2. Comparison between simulated and measured soil moisture in the top 60 cm of profile under a finger millet crop in plot 1.

rainfall was the dominant feature in both the plots and accounted for more than 50% of the irrigation and rainfall input. While groundwater recharge from both the plots amounted to about 12% of the input, ET accounted for about 37%. The overall responses of both the plots were similar during the wet season. The dry season responses, however, exhibited dependence on the crop type. While the recharge component formed about 22% of the irrigation input for the shallow-rooted ladies finger crop, it was virtually absent for the mulberry crop.

3.4. Simulation model CRISHI

Based on the knowledge gained from the field experiment, a simple, conceptual model called CRISHI has been developed, which simulates the behaviour of the soil vegetation system under water input. The model performs well in spite of its simplicity (Fig. 2). A sensitivity analysis indicated the insensitivity of CRISHI to the choice of certain empirical input parameters bringing out the importance of accurate potential ET computations.

References

1. DOORENBOS, J. AND PRUITT, W. O.
   Guidelines for predicting crop water requirements, FAO Irrigation and Drainage Paper, No. 24, UN, Rome, 1977

2. VAN GENUCHTEN, M. TH.
   A closed-form equation for predicting the hydraulic conductivity of unsaturated soils, Soil Sci. Soc. Am. J., 1980, 44, 892–898

3. BROOKS, R. H. AND COREY, A. T.
   Hydraulic properties of porous media, Hydrology Paper No. 3, Colorado State University, Fort Collins, Colorado, 1964, p. 27.

4. CAMPBELL, G. S.
   A simple method for determining unsaturated conductivity from moisture retention data, Soil Sci., 1974, 117, 311–314.

Thesis Abstract (Ph. D.)
Towards optimal synthesis of articulated manipulators with joint motion constraints
by T. A. Dwarakanath
Research supervisors: U. Shrinivasa and A. Ghosal
Department: Mechanical Engineering

1. Workspace analysis

The thesis deals with kinematic and dynamic analysis and design of articulated manipulators (Fig. 1) with joint motion constraint[1,2]. Due to interference, stroke length limitations and other reasons, motion constraints exist at the joints. The workspace becomes significantly different from the case without constraints. Therefore, the four Denavit–Hartenberg parameters are not sufficient to describe the kinematics with joint motion constraints. We introduce two additional parameters, namely, the range of joint motion, θ_{jr}, and the mean position of the range, θ_{jm}. We use these with the earlier four parameters to describe the workspace geometry. The expressions for θ_{jr} and θ_{jm} in terms of extreme values of joint variables θ_j are as follows:

$$\theta_{jr} = \theta_{j\,\text{max}} - \theta_{j\,\text{min}}$$

$$\theta_{jm} = \left(\theta_{j\,\text{max}} + \theta_{j\,\text{min}}\right)/2 \quad j = 1,..,n.$$
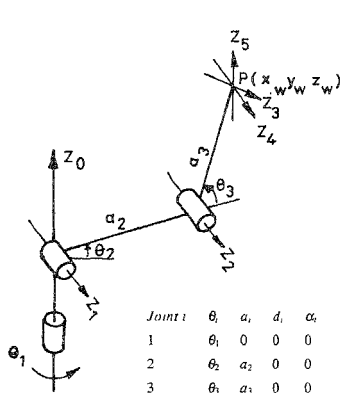
FIG. 1. An articulated manipulator .   FIG. 2. Section in Y_0–Z_0 plane.
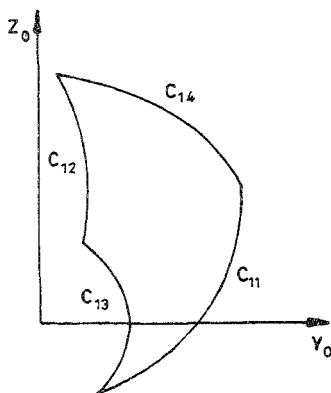
We classify the workspace geometry according to the mean positions of the joint rotation ranges. We show that all possible geometries can be obtained from simple building blocks referred to as Case 1 in the thesis. We obtain this when $\theta_{3_m} \neq 0$, θ_{3_m} and θ_{3_r} are such that θ_3 cannot take or cross a value 0 or π; here we get only four surface segments (Fig. 2). They correspond to extreme values of θ_2 and θ_3. The following subsections deal with kinematic characteristics of such geometry.

1.1. Section area

We use the kinematic characteristics—sectional area and workspace volume—as indices for evaluating the performance. The sectional area is obtained when we cut the workspace by a plane containing Z_0 axis and it has four curves in Case 1. The expression for sectional area in terms of mean positions and ranges of θ_2 and θ_3 is

$$A_s = 2a_2 a_3 \left(\theta_{2_r}\right) \sin\left(\theta_{3_m}\right) \sin\left(\theta_{3_r}/2\right) \qquad ($$

where a_i, $i = 1, 2$ are link dimensions.

1.2. Workspace volume

We obtain the workspace volume as a solid of partial rotation of the sectional area. The expression for the volume is

$$V = (1/2)\theta_1, \sin\left(\theta_{2_r}/2\right)$$
$$\times \left[2a_2 a_3^2 \left(\theta_{3_r} \sin\theta_{2_m} - \sin\theta_{3_r} \sin\left(2\theta_{3_m} + \theta_{2_m}\right)\right) \right]$$

$$-8a_2^2 a_3 \cos\theta_{2_m} \sin\theta_{3_m} \sin\left(\theta_{3_m}/2\right)\Big].$$ (2)

In addition, we introduce a characteristic called the work area that is often of interest in applications like painting and welding. The existence of multiple inverse kinematic solutions in the workspace is important in several applications. We identify the conditions leading to their occurrence.

2. Workspace utilization

To accommodate a given workpiece, geometry (or shape) is sometimes more important than the workspace volume. It is very useful for a designer to know the optimum values of the design parameters to embed a given workpiece of complex geometry. We develop algorithms to find the largest rectangular area. We also obtain the largest solids, such as rectangular box, the cylinder and the sphere that can be embedded in the workspace. The algorithm to find the maximum area of the rectangular surface or volume of a given object that can be embedded in the workspace, W_k, makes use of the nature of boundary surfaces and checks interference of the object with the boundaries at the given position. If we could denote both the geometry and the volume of the object by symbol O_b then, $O_b \subseteqq W_k$. We then increase the object until the above condition fails to satisfy to obtain the optimum object volume. The algorithms are useful to synthesize link dimensions optimally when a given workpiece has to be embedded.

A method has been proposed to design manipulators for applications such as painting and welding. The procedure exploits the results obtained above and incorporates process specifications of the applications and yields the dimensions of the manipulator and the mean positions of the joint ranges.

3. Dynamic analysis

The influence of different design parameters on torque requirements at the joints to perform a specific task has been brought out. In the kinematic design, the main design parameters are the link lengths, mean positions and ranges of joint motions. Apart from these, several other parameters need to be considered to analyse the dynamic performance of a robotic system.

The cross-sectional dimensions of a link are designed by considering the worst loading condition on the link in the entire process of painting or welding. The various loads on the link are the static loads of payload, actuators and transmission elements, the self weights of the links, and the dynamic loads due to the motion of the manipulator. In this work we use tubular links, which not only reduce the weight of the system but can serve also as conduits for the electrical cables. A criterion based on the permissible maximum deflection at the end effector and allowable stress at the critical section is used to choose the cross section of the link.

The torque required to drive the arms at specified velocities and accelerations can be found once the kinematic and mass properties are known. A procedure is presented to select the optimum drive system to provide the required torque such that the combined weights of the motors and the transmissions are small. Finally, a minimization of torque requirements with respect to link ratios, joint ranges and mean positions is done.

$$\text{Find Min}\left(\sum_{i=1}^{i=3}|\tau_i|\right)$$

subject to the following constraints:

$$G_1 : \tau = f_1\left(l_r, a_p, \bar{\theta}_m, \bar{\theta}_r, m_{(m+t)}, a_2, m_p, m_t, \beta\right) \quad \text{---Torque requirement}$$

$$G_2 : A_r = f_2\left(A_d, \beta, a_p, v_p\right) \quad \text{---Area requirement}$$

$$G_3 : a_2 = f_3\left(l_r, \bar{\theta}_m, \bar{\theta}_r, A_r\right) \quad \text{---Dimensional synthesis}$$

$$G_4 : \delta = f_4\left(l_r, \bar{\theta}_m, \bar{\theta}_r, m_{(m+t)}, a_2, m_p, m_t\right) \quad \text{---End-point accuracy}$$

where τ is the torque required to drive the links at required acceleration and speed. l_r is the link ratio, $(a_2/(a_2 + a_3))$. a_p are v_p are end-effector acceleration and velocity, respectively. $m_{(m+t)}$ is mass of motor and transmission assembly. m_p and m_t are masses of payload and link i, respectively. A_d is the desired area to be painted and A_t is area required in the robotic workspace to accommodate the desired area. β is the trajectory of the end effector and δ is the end-effector accuracy.

This optimization results in design of smaller and lighter articulated manipulators. Several numerical examples and design charts[1,2] are presented in the thesis which can be used for optimal synthesis.

4. Conclusions

The thesis deals with the kinematic and dynamic analysis and optimal design of articulated manipulators with joint motion constraints. For their design both kinematic and dynamic criteria are considered. The thesis ascertains that joint motion limitation significantly alters kinematic and dynamic performance. Ignoring such restrictions in design stage may result in the manipulator becoming unsuitable for the purpose intended. Considering the joint motion limitations would lead to accurate information about the workspace and optimum design and use of the entire robotic workcell.

References

1   DWARAKANATH, T A., GHOSAL, A. AND   Workspace and kinematic design of manipulators with joint
    SHRINIVASA, U.   motion constraints, *Proc ASME* 1992 *Mechanisms Conf.*
                                         Arizona, USA, 1992.

2. DWARAKANATH, T. A., GHOSAL, A. AND   Design of articulated manipulator based on workspace and
    SHRINIVASA, U.   dynamic criteria, *Proc. ASME* 1992 *Mechanisms Conf.*,
                                         Arizona, USA, 1992.

Thesis Abstract (Ph.D.)
Time domain analysis of engine exhaust systems with perforated element mufflers by
M. N. Kumar
Research supervisor: M. V. Narasimhan
Department: Mechanical Engineering

1. Introduction

The improvement in engine design and development is measured, more often than not, in terms of the brake power per litre of displacement. In order to improve the performance, it is imperative

that the air flow rate through the engine, characterised by volumetric efficiency, should be improved. The gas exchange processes, *i.e.*, charging the cylinder with fresh air through an intake system and discharging the exhaust gases into atmosphere through the exhaust system, govern the volumetric efficiency of the engine. The other important aspect of the gas exchange process is exhaust noise which is attenuated using mufflers. However, mufflers also significantly influence the exchange processes.

The most sophisticated analysis of gas exchange processes would involve modelling of the unsteady flow through the intake and exhaust system which contain a number of flow-restrictive devices. To evaluate the pressure waves in the exhaust and intake systems, unsteady conservation equations are to be solved. In available literature, the solutions have been obtained with and without linearising the governing equations. However, it has been found recently that linearised governing equations have limited application for the analysis of internal combustion engine exhaust systems. In nonlinear analysis, termed as time-domain analysis in literature, the governing equations are converted into characteristic equations and the solution is obtained using numerical methods. Three different types of numerical schemes are used in literature. The first part of the investigation deals with comparative evaluation of the numerical schemes used as a solution for the characteristic equations.

Of the various types of mufflers used for suppression of exhaust noise, perforated element mufflers are known to offer high insertion loss and low back pressure. In fact, most of the modern automobiles introduced in India in recent years use perforated element mufflers. The perforated element mufflers have been analysed in frequency-domain analysis by earlier investigators[1]. As this analysis has limited role in the analysis of exhaust systems, in the second part of the investigation, time-domain analysis of perforated element mufflers has been attempted.

2. Comparative evaluation of numerical schemes used for the solution of characteristic equations

In the method of characteristics, one-dimensional unsteady conservation equations are initially transformed into characteristic equations,

$$d\lambda = dA + \frac{\gamma - 1}{2}dU = \frac{A}{A_0}dA_0 \text{ along the path } \frac{dX}{dZ} = U + A \quad (1)$$

$$d\beta = dA - \frac{\gamma - 1}{2}dU = \frac{A}{A_0}dA_0 \text{ along the path } \frac{dX}{dZ} = U - A \quad (2)$$

and

$$dA_0 = 0 \text{ along the path } \frac{dX}{dZ} = U, \quad (3)$$

respectively, where γ is the ratio of specific heats of exhaust gas, A, nondimensional acoustic speed, and U, the nondimensional velocity, and characteristic variables λ, β and A_0 are evaluated in the solution domain using an appropriate numerical scheme. X and Z are nondimensional distance and time, respectively.

Before the advent of digital computers, the characteristic equations were solved using graphical method. Jones[2] implemented the graphical method on digital computers and claimed that it predicts exhaust noise spectrum more accurately than other methods. Benson *et al.*[3] proposed the first computer-based algorithm as a solution for the characteristic equations, termed in this investigation as semigrid method. The method is a mixture of the graphical and grid methods of solutions. Benson *et al.*[3] claimed that graphical method of solving the entropy characteristic re-

sults in more accurate results. More recent investigators, such as Munjal[1], have used the pure grid method. This method is much simpler to implement on computers compared to other methods. In literature, these methods have not been compared in relation to the analysis of typical exhaust systems. In this investigation, these three methods have been implemented.

A four-stroke engine with uniform exhaust pipe with no tail pipe has been selected, as a case study, neglecting friction and heat transfer. These methods have been compared with respect to tail pipe velocity which is directly related to exhaust noise and cylinder pressure which is related to engine performance. The tail pipe velocity computed by different methods for an exhaust pipe length of 0.65 m is shown in Fig. 1. It can be seen that the computed tail pipe velocity differs marginally. The cylinder pressure computed by different methods is shown in Fig. 2 for the same exhaust pipe. It has been observed that the differences are marginal for a different exhaust pipe of length 1.3 m also. In Table I, the computational time required for different methods in the case of a 0.65 m exhaust pipe is shown.

Thus, based on computational time and ease of implementation, it is concluded that the uniform grid is preferable to other methods.

3. Time-domain analysis of perforated element mufflers

Perforated element mufflers are often used in engines to attenuate exhaust noise. These mufflers have been analysed hitherto in the frequency domain, with and without mean flow by earlier investigators. In this part of the investigation, time-domain analysis of perforated element mufflers under actual operating conditions is presented, where mean flow is not uniform with time and strong irreversibilities are present along with finite-amplitude pressure waves.

When a pressure wave moves along the perforated duct, the mass is transferred through perforations either from the outside to the perforated duct or from the perforated duct to the outside
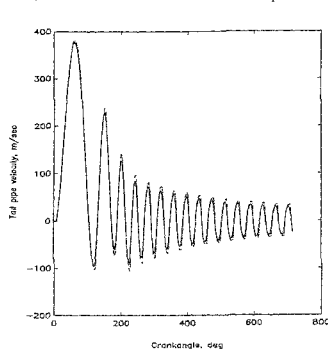

FIG. 1. The tail pipe velocity of 0.65 m exhaust pipe computed from different methods of numerical solution. —: wavediagram method; ---: uniform grid method, and :–: semigrid method.
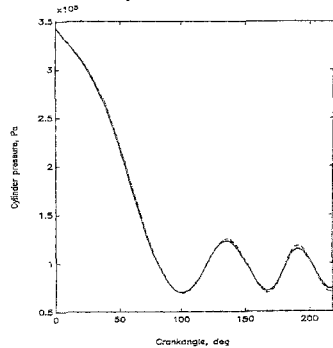
FIG. 2. The cylinder pressure with 0.65 m exhaust pipe computed from different methods of numerical solution —: wavediagram method; ---: uniform grid method, and :–: semigrid method.

Table 1
Computational time required for three cycles

Method	Computer time
Wavediagram	92 m 23 s
Semigrid	1 m 42 s
Uniform grid	1 m 23 s

depending upon the pressure gradient across the perforation. This mass transfer results in attenuation of the pressure wave. Thus the governing equations of the pressure wave in the perforated duct should take into account mass transfer through the perforation. If the mass transfer in the perforate in both directions is considered, then the unsteady conservation equations can be derived from first principles as

$$\frac{\partial p}{\partial t} + \rho \frac{\partial u}{\partial x} + u \frac{\partial p}{\partial x} + \frac{\rho u}{F} \frac{dF}{dx} - \frac{\dot{m}_y}{F} = 0 \tag{4}$$

$$\frac{1}{\rho} \frac{\partial p}{\partial x} + \frac{\partial u}{\partial t} + u \frac{\partial u}{\partial x} + G + u \frac{\dot{m}_y}{F\rho} = 0 \tag{5}$$

$$\frac{Dp}{Dt} - a^2 \frac{D\rho}{Dt} - (k-1)\rho \left(q + uG + \dot{m}_y \left\{ \frac{E_{ys} - E_{xi}}{\rho F} + \frac{u^2}{\rho F} \right\} \right) + \frac{(k-1)a^2}{kF} \dot{m}_y = 0 \tag{6}$$

where E_{ys} is stagnation enthalpy and E_{xi}, the internal energy and dynamic head of the mass in the pipe. It may be observed that the mass flow through perforation affects all conservation equations. For example, positive pressure results in $+\dot{m}_y$ and this has the same effect as that of a diverging pipe which is known to attenuate positive pressure wave.

It may be noted that the term $\dot{m}_y$ should be known throughout the solution domain for the solution of the governing equations. Acoustical mass flow through the perforate has been extensively studied by previous investigators. Cummings has used a semianalytical model to represent linear and nonlinear behaviour of the flow through perforate[4]. Using this model, it can be shown that the flow through perforates of engine mufflers can be approximated to quasisteady flow. This observation is further substantiated by the observation of Patton and Goldman[5] that the flow through the perforate can be considered as quasisteady if the magnitude of the amplitude of the oscillating particle has the same order of magnitude as the diameter of the perforate. In this investigation, the mass flow rate through perforate has been computed based on the static pressure difference and upstream temperature while considering the compressibility effect of the exhaust gas.

The method of characteristics has the inherent capability to exploit the hyperbolic nature of the unsteady conservation equations to obtain an accurate solution and is adopted in this investigation also.

The proposed time-domain model of the perforated element has been used to examine two types of perforated element mufflers, concentric resonator and Plug-type mufflers.

3.1. *Concentric resonator*

The simplest configuration of the perforated element mufflers is the concentric resonator shown in Fig. 3. In the analysis of concentric resonator, the nonlinear pressure waves in the outer and
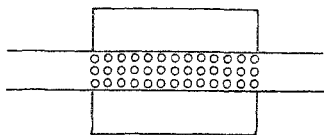
FIG. 3. Concentric resonator.

FIG. 4. Experimental corroboration of the computed pressures in the outer duct of the concentric resonator. —: Analytical, and ---: Experimental.

inner ducts have been considered and are coupled with mass flow through the perforation at different sections of the muffler. As the outer duct of the muffler has closed boundaries, particle velocity at these boundaries has been set to null. At tail pipe boundary of the muffler, the constant pressure model has been used. At the other boundary, *i e.*, the muffler and exhaust pipe junction, the strength of the characteristic traveling from the perforated pipe is compensated by the presence of perforations, heat transfer and friction while that from the exhaust pipe is compensated for heat transfer and friction only.

A Fortran program has been developed to simulate an exhaust system of a four-stroke engine with a concentric resonator type of muffler. The coupled conservation equations or coupled characteristic equations in the muffler are solved using forward differencing scheme. It has been found that the grid size required for the simulation of the perforated element muffler is much smaller than that of the simple exhaust pipe as the rate of attenuation of the pressure waves is very high. It has been attempted to corroborate the computed pressure history in concentric resonator muffler of a 5 H. P. diesel engine (Fig. 4). It may be observed that the experimental and analytical pressure traces show similar trends such as number of peaks, attenuation of pressure wave amplitude and complete suppression of pressure waves over a period of 360°, *i e.*, half the cycle time. However, the amplitude of the reflected pressure wave due to blowdown pressure encountering the tail pipe seems to have been overestimated.

3.2. *Plug muffler*

The plug muffler is a complicated perforated element muffler (Fig. 5). Its most important feature is that the entire exhaust gas enters the outer duct whereas in the concentric resonator it enters partially only. In the analysis of plug muffler, pressure waves in all the ducts of the mufflers are considered. Two additional boundaries are to be considered compared to concentric resonator, *i.e.*, the gas velocities on both sides of the plug are to be set to null.

Another program was developed to simulate the exhaust system of a four-stroke engine with plug muffler. The coupled conservation equations in the inner and outer ducts of the plug muffler
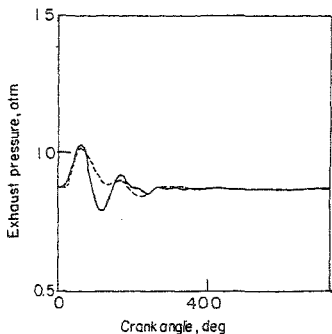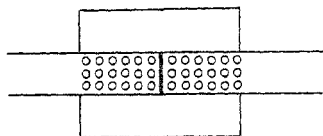
FIG. 5. Plug muffler.
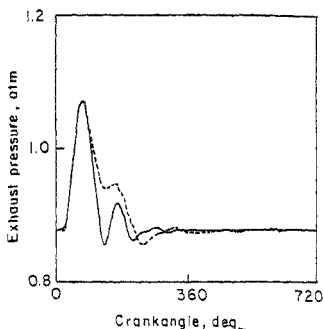
FIG 6 Experimental corroboration of the computed pressures in the outer duct of the plug-type muffler. —: Analytical, and ---: Experimental.

have been solved as in the case of the concentric resonator. The computed and experimental pressure histories at the mid-point of the outer duct of the plug muffler have been shown in Fig. 6. Although there is some mismatch with respect to amplitude and phase, similar features can be observed in both pressure time histories.

4. Conclusions

(i) Based on a comparative study of the numerical schemes used for the solution of characteristic equations, it is concluded that the differences between the methods are marginal. Based on the computational time and ease of implementation, the uniform grid method is preferable to the other methods.

(ii) Based on the semianalytical model, it has been found that the flow through a perforate can be assumed to be quasisteady for the time-domain analysis of the perforated element mufflers of internal combustion engines.

(iii) Based on the corroboration of the experimental and analytical pressure histories in the exhaust system with perforated element mufflers, it is concluded that the proposed one-dimensional perforated element model is satisfactory.

References

1. MUNJAL, M. L.   *Acoustics of ducts and mufflers*, 1987, Wiley.

2. JONES, A. D.   *Noise characteristics and exhaust process gas dynamics of a small 2-stroke engine*, Ph. D. Thesis, University of Adelaide, 1978.

3. BENSON, R. S., GARG, R. D. AND   A numerical solution of unsteady flow problems, *Int. J WOOLATT, D.   Mech. Sci*, 1964, **6**, 117–144.

4. CUMMINGS, A.   The response of a resonator under a turbulent boundary layer to a high amplitude non-harmonic sound field, *J. Sound Vib.*, 1987, **115**, 321–328.

5. PATTON, R. L. AND GOLDMAN, A. L.   Correlation of nonlinear orifice impedance, *J. Acoust Soc. Am.*, 1976, **60**, 1390–1396.

Thesis Abstract (Ph. D.)
Flow characteristics in the stalled region of a high specific speed axial impeller by
P. A. Rajan
Research supervisors: S. Soundranayagam and M. V. Narasimhan
Department: Mechanical Engineering

1. Introduction

Correlations and descriptions of stalled flow in axial compressors based on tests on high hub-to-tip diameter ratio machines[1] may not be similar in many respects to stall in axial impellers in general. Impellers of low hub-to-tip diameter ratio may be expected to be dominated more by three-dimensional effects and have a more complicated stalled flow behaviour. Measurements are made in an axial impeller of hub-to-tip diameter ratio of 0.5 designed for a nominal flow coefficient $\phi = 0.5$.

2. Experimental

The impeller, of free vortex design, was of diameter 581 mm (15″) and had 20 blades of IOC4 blading, the blade camber varying from 30° at the root to 10° at the tip. The blade stagger varied from 24° at the root to 58° at the tip. The impeller was housed in an annular duct with the flow being controlled by a simple flat plate throttle, the air leaving radially through a flared axisymmetric exhaust bell. All the tests were run at low speeds with the impeller running at 3000 rpm.

Detailed measurements of the flow and pressure distributions were made using four-hole combination yaw-pitch probes as well as hot wires. The three components of velocity in the unsteady flow regime were measured using a single rotated inclined hot-wire probe[2]. The hot-wire signals were phase-lock averaged with respect to impeller or the stall cell rotation to eliminate, to a possible extent, the effect of random fluctuations.

3. Results and discussion

The shape of the cells was determined from phase-lock-averaged hot-wire signals taken at different radii, all of them individually related to simultaneous signals from a reference wire at midspan. The most surprising and unexpected result was that near the hub the axial velocity within the cell increased to values above that in the unstalled region.

The longitudinal configuration of the cell in the annulus was determined by examining the simultaneous traces of pairs of hot wires oriented at stations two chords upstream to seven chords downstream of the impeller. In this way, the time lag of any downstream station with respect to an upstream station could be estimated, and hence the lateral circumferential displacement of the cell at any axial station (Fig. 1). The points lie along well-defined straight lines suggesting a
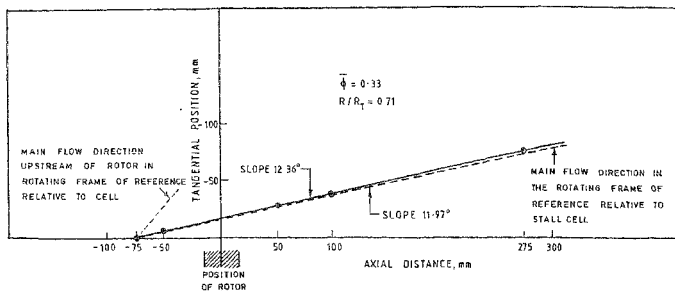
FIG 1   Stall cell configuration along the axis of the impeller

helical alignment of the cell. The figure also shows the main direction downstream of the impeller in a rotating frame of reference relative to the stall cell, the direction of the main flow being determined from yaw probe measurements. The close agreement between the alignment of the stall cell and the main flow in a cell-referenced frame indicates that in this frame the flow in the cell and the main flow is parallel to one another without crossing of the cell boundaries, or that the cell behaves as a wake of a bluff body.

It was possible to obtain information on the formation and disappearance of the stall cells by examining the unaveraged traces of the hot-wire signals as the impeller went into or came out of stall. The width and spacing of the incipient cells yielded information about their growth and speed as they grew to full size. During stall initiation the propagation speed settles down to its ultimate value of 0.61 rotor speed in about 8 rotor revolutions. However, it takes 25 rotor revolutions for the cell to grow to its steady size.

The flow within the stall cells was qualitatively not very different from that outside the cells. The relative flow outlet angle within the cell plotted as a function of the local flow coefficient shows that the blade profile behaves as expected at the local flow coefficient, or local incidence, whether inside or outside the cell.

The level of velocity fluctuations within a stall cell is again not very different from that in the clean flow outside it. The average level of fluctuation varied from about 8% at the casing to 2% at the hub. The unstalled portions of the stalled flow are found to operate at much larger coefficients than implied in the stall models.

4. Conclusions

The picture of stall that emerges from the present study is of the stall cell being a relatively large area of reduced flow but without the axial velocities falling to very low values such as in a dead zone. The fractional area of the cell is larger than the effective blockage, this being confirmed by the level of measured axial velocities within the cell. An unexpected finding was the existence of a jet-like flow within the cell at the root, the fluid in the high-velocity jet being identified by its high total pressure as migrating radially inwards from the tip reversal region.

The value of critical blockage for the existence of full span stall is much smaller than the value of 30% suggested by the correlations. The effective ϕ of the unstalled portion of the flow outside the cell is much larger than that corresponding to the stalled ψ_{T-S} value. The stall cell has a spiral configuration which is oriented parallel to the main flow streamlines in a frame of reference moving with the cell. This implies no transverse motion of the external flow through the cell, as assumed in models that postulate an axial cell orientation.

The flow within the cell is not radically different from the external flow. Measurements show that the relative flow outlet angles within the cell conform to the expected pattern corresponding to the local flow coefficients. The stall cells appear to start near the tip. Tip blockage increases the velocity levels nearer the hub helping to stabilize the flow in the lower part of the span.

Transient measurements show that the stall cell reaches its final velocity after inception in about 8 revolutions of the rotor, though it takes about 25 rotor revolutions for the cell to attain its final size. The change in cell speed and size during cessation of stall is the mirror image of the starting process.

References

1. DAY, I. J.   Detailed flow measurements during rotating stall in axial flow compressors, AGARD CP 177, *Unsteady flow in turbomachinery*, 1976.

2. WHITEFIELD, C. E., KELLY, J. C. AND BARRY, B. A.   *Three-dimensional analysis of rotor wakes*, 1972, Aew Quest.

Thesis Abstract (Ph. D.)
Frictional-kinetic models for steady cohesionless granular flow through a wedge-shaped hopper by Jyotsna Ramasubbu
Research supervisor: K. Kesava Rao
Department: Chemical Engineering

1. Introduction

The present work attempts to combine a newly developed kinetic constitutive theory with an older frictional theory to model the two-dimensional gravity flow of a cohesionless granular material such as sand through a wedge-shaped hopper. Frictional theories work best for slow flows and high bulk densities, when the constituent grains are in sustained contact with each other as they flow. On the other hand, kinetic theories have been developed for fast flows at low bulk densities, when the particles no longer maintain sustained contact with each other.

The present work is motivated by the fact that earlier frictional flow models used to describe hopper flow, fail to give a physically reasonable solution near the hopper exit. The solution is not continuous across the exit, and discharge rates predicted are invariably higher than the experimental values. The idea of modifying the constitutive equations to include kinetic effects is suggested by density measurements reported in the literature. They show that the material dilates as it flows down the hopper, assuming values of density near the exit below which it is no longer reasonable to assume that friction alone is the mechanism of stress build up. Therefore, a com-

bined frictional-kinetic theory is used here to model the flow in the upper regions of the hopper, as well as near the exit.

2. Results

The equations are first tested on an imcompressible one-dimensional approximation called the smooth-wall, radial gravity problem. As a result of simplifying assumptions, the governing partial differential equations are reduced to ordinary differential equations. When they are suitably non-dimensionalised, the pseudo-thermal energy balance is decoupled from the momentum balance. Further, a small parameter ε multiplies the kinetic stress term in the momentum balance, and the conduction term in the energy balance. The energy balance is first solved using the method of matched asymptotic expansions. The temperature profile so obtained is then used to solve the momentum balance by a regular perturbation method. The results appear to justify the inclusion of kinetic stresses in the model, since they are found to dominate in the region of the exit. Further, the discharge rate predicted is lower than the purely frictional value. However, since the kinetic terms are multiplied by ε, their effects are not felt quantitatively. Nevertheless, the approach is extended to the realistic hopper problem, in the hope that with the inclusion of compressibility and a two-dimensional model, the kinetic effects will be large enough to overcome the problems with the purely frictional equations.

For the compressible two-dimensional model, the particle jet below the hopper is included in the analysis, and downstream conditions are specified far below the hopper exit. Here too, the kinetic stress terms in the momentum balance are multiplied by a small parameter ε'. The governing equations and boundary conditions are highly nonlinear, and resist solution. They are simplified further by quasi one-dimensionalisation. Simple transverse profiles are assumed for the variables, and the equations are integrated along the hopper cross section. The resulting equations are solved in two regions. In the upper region of the hopper, the frictional limit of the equations is solved as an initial-value problem. These equations break down when the density decreases to the value corresponding to the loosest packing of spheres. The frictional-kinetic equations are then solved below as a boundary-value problem. This nonlinear problem is also very difficult to solve, and is therefore simplified by linearisation. The solution finally obtained reveals some interesting features, but is not entirely satisfactory. The most encouraging result is that it is possible to obtain a continuous solution across the hopper exit that goes smoothly from the frictional solution in
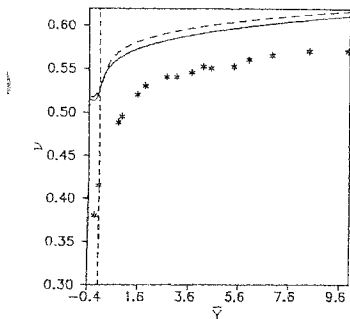

FIG. 1. Density profiles for glass beads at two wall angles, compared with the data of Fikie et al.[1] (* * *) : (— — —) $\theta_w = 5°$, (——) $\theta_w = 10°$.

the hopper to free fall in the jet. The material dilates for a little distance below the hopper, but compacts later. This is not a serious drawback, since compaction could have been prevented if the transverse kinetic stress gradients had been large enough to counter the converging inertial flow, and the particle trajectories had moved to vertical paths. Further, the density profile in the hopper is qualitatively similar to the experimental profile of Fickie et al.[1] (Fig. 1). Thus it is concluded that the inclusion of kinetic effects in a frictional model helps to obtain a continuous solution across the hopper exit. However, in order to predict the experimentally observed dilation in the jet, it appears that either the model must be modified to include transverse gradients, or a superior kinetic theory must be employed, since the present one was developed for small mean field gradients.

Reference

1. FICKIE, K. E., MEHRABI, R, AND   Density variations in a granular material flowing from a wedge-
   JACKSON, R.   shaped hopper, *AIChE J.*, 1989, **35**, 353–355.

Thesis Abstract (Ph. D.)
Influence of impurities and alloying additions on the processing maps for hot working of nickel and nickel-base superalloys (Ni, Ni-C, Ni-C-S, Ni-20Cr, IN 600, IN 718, Nimonic 75, 80A and 90) by N. Srinivasan
Research supervisor: Y. V. R. K. Prasad
Department: Metallurgy

1. Introduction

Nickel-base superalloys are used for gas turbine components like turbine disks, blades and vanes. Because of demanding service conditions like high temperature, dynamic stress, corrosion and oxidation, it is necessary that the microstructure is carefully controlled. High-temperature strength in the superalloys is achieved through ordered coherent γ' precipitation although microstructural control through thermomechanical processing is recognized to play a very important role. For shaping the superalloys, high-temperature deformation is essential so that the strengthening phases (γ' and/or γ'') are in solution. For the purpose of optimizing the hot workability and controlling the microstructure during mechanical processing, it is necessary to understand the constitutive flow behaviour under hot working conditions and characterize the microstructural mechanisms. The aim of the present investigation is to evaluate the constitutive flow behaviour of some nickel-base materials at temperatures and strain rates relevant to hot-processing operations. This study will lead to an understanding of the mechanisms of hot deformation and to achieving microstructural control without the occurrence of microstructural damage or unstable flow.

The approach of developing processing maps[1] has been adopted in this investigation since the kinetic approach for analyzing the hot deformation characteristics is inadequate for understanding the dynamic behaviour of the material. The processing maps represent the instantaneous power dissipation given by $2m/(m + 1)$, where m is the strain rate sensitivity. The variation of efficiency with temperature and strain rate is represented in the form of an iso-efficiency contour map which exhibits different domains representing specific microstructural processes. For hot working, the domain of dynamic recrystallization (DRX) is preferred since this imparts high intrinsic workability to the material. From the processing maps, a combination of temperature and strain rate leading to optimum intrinsic workability may be obtained and microstructural control achieved by

controlling the process parameters such that they are in the domain of DRX. The continuum instability criterion developed on the basis of the principle of maximum rate of entropy production is used to delineate regimes of unstable flow in the processing map. In this investigation, processing map for the base metal (pure nickel) has been first established followed by binary Ni–Cr and ternary Ni–Cr–Fe such that a fundamental understanding may be developed on the hot deformation behaviour of more complex alloys like IN 718 and the Nimonic series. Further the role of impurities like carbon and sulphur on the behaviour of the superalloys is examined through a study of their effect on pure nickel.

2. Experimental

The materials investigated in this study were pure nickel (99.98%), nickel containing trace elements of carbon and sulphur, Nichrome (Ni-20Cr), IN 600, IN 718, Nimonic 75, 80A and 90. Cylindrical specimens with a height-to-diameter ratio of 1.5 were used for hot compression testing which was chosen in view of the ease with which constant true strain rate can be achieved by an exponential decay of actuator speed. Testing was conducted on a DARTEC servohydraulic machine in the entire hot working temperature range of each material and true strain rate range of $0.001–100 \text{ s}^{-1}$. The deformed samples were quenched from the test temperature and examined using optical microscopic techniques. On the basis of the flow stress data as a function of temperature, strain and strain rate, power dissipation maps were developed using a computer software.

3. Results

The processing map for pure nickel exhibits a DRX domain with a peak efficiency of 31% occurring at 925°C and 1 s^{-1}. Addition of 0.02 wt% carbon has shifted the DRX domain on the strain rate axis to a much lower strain rate of about 0.0003 s^{-1} without significantly affecting the DRX temperature. The peak efficiency has however increased to 44%. On the basis of a simple DRX model which considers rate of nucleation vs rate of growth, it is shown that DRX in nickel is controlled by the rate of nucleation which depends on thermal recovery by climb. This is similar to that in copper which is also a low-stacking fault energy material. Interstitial carbon is very effective in pinning the dislocations and increasing the rate of dislocation generation and therefore the DRX nucleation occurs at lower strain rates. The presence of sulphur to the extent of 0.002 wt% gives rise to a high-temperature domain at 1200°C and 0.0003 s^{-1} with a high efficiency of about 60%. This domain has been identified to represent wedge-cracking process.

The processing map of Ni-20Cr exhibited a DRX domain with a peak efficiency of 38% occurring at 1200°C and 0.1 s^{-1}. The higher DRX temperature in this alloy is attributed to the long-range back stress caused by solid solution strengthening by chromium. The material also exhibits a grain boundary cracking domain at temperatures lower than 900°C and strain rates lower than 0.001 s^{-1}. The Ni-Cr-Fe alloy (IN 600) undergoes DRX with a peak efficiency of 48% occurring at 1200°C and 0.2 s^{-1}. The DRX domain, however, shrinks in this alloy in comparison with that in Ni-Cr alloy. Furthermore, IN 600 exhibits intercrystalline cracking at temperatures higher than about 1150°C. Thus the effect of iron on the hot deformation of Ni-Cr alloys is essentially to narrow down the hot working temperature and strain rate ranges and to induce intercrystalline cracking at high temperatures.

The map for the nickel-iron-base superalloy IN 718 exhibits two different DRX domains separated by the temperature for the δ phase (Ni_3Nb) dissolution (1040°C). The lower temperature DRX domain has a peak efficiency of 37% occurring at 950°C and 0.001 s^{-1}. In this domain very

fine-grained uniform microstructure is developed during processing. The higher temperature DRX domain has a peak efficiency of 40% occurring at 1200°C and 0.1 s^{-1}. Hot working of this material in the initial stages is best done at 1200°C and 0.1 s^{-1} since the workability will be more and the working loads less. The resulting grain size, however, will be larger than that obtained by forging in the lower temperature DRX domain. Finishing operations may, however, be done at lower temperatures since fine grain sizes are preferred for good LCF properties of components like a turbine disk. The map has also revealed that the DRX domain at higher temperatures is limited to strain rates less than 1 s^{-1} since intercrystalline cracking predominates at higher strain rates.

The processing maps for the Nimonic series of alloys 75, 80A and 90 have very similar features and exhibited a single high-temperature DRX domain with a peak efficiency of about 38% occurring at 0.1 s^{-1} and at temperatures of about 1200, 1150 and 1130°C, respectively. A careful examination of the maps revealed that the DRX domain occurs at temperatures above that for carbide dissolution. Also, the domain at the peak efficiency is narrower in the order of Nimonic 75, 80A and 90, indicating that the hot workability range is more restricted in that order. The addition of cobalt in Nimonic 90 increases the solubility of carbon in the γ solid solution and widens the temperature range for DRX to include lower temperatures.

All the nickel-base materials studied in this investigation have exhibited flow instabilities at strain rates above 1 s^{-1}. These instabilities are manifested as adiabatic shear bands in the microstructure. Another general feature is the occurrence of intercrystalline fractures at temperatures higher than 1150°C and strain rates above 1 s^{-1}. All these regions may be avoided in processing nickel-base materials.

4. Conclusion

The present investigation has clearly demonstrated that the technique of processing map is very valuable in optimizing the hot workability and controlling the microstructure of nickel-base superalloys. The technique has also brought out the exact influences of impurities like C and S and that of alloying elements like Nb in IN 718 and Co in Nimonic 90 on the hot working characteristics.

Reference

1. PRASAD, Y. V. R K , et al   Metall Trans A, 1984, 15, 1883-1893.

Thesis Abstract (Ph. D.)
Rotating crucible electron beam evaporation technique for mixed oxide films by
L. Shivalingappa
Research supervisors: S. Mohan and K. Narasimha Rao
Department: Instrumentation and Services Unit

1. Introduction

The requirement for new materials with a wide range of properties to meet the ever-increasing demand for thin-film devices has been fulfilled only partially by depositing them in thin film form and tailoring them by controlling the deposition conditions. The synthesis of thin film of multicomponent materials has further extended this range of materials.

Though mixing the constituents in the required proportion and using the mixture as the starting material to prepare these multicomponent films is the simplest form of preparing these multicomponent films, the difference between the vapour pressures of constituents does not permit the films to have the same composition as that of the starting material. Techniques such as flash evaporation and jumping electron beam evaporation could not solve the problems completely. Multisource deposition using either resistive or electron beam guns or sputtering targets offered more flexibility, though more space was required in the vacuum chamber to accommodate these subsystems resulting in more expensive and complicated systems. As such, they could find limited applications in industry. As a result, the innovations and modifications to the deposition techniques continued for preparing films with controlled stoichiometry. In this work. we have used a single electron beam gun which is provided with rotation of the crucible which has sectors filled with different materials. The versatility of this technique has been tested by preparing homogeneous and graded index films from CeO_2 and SiO_2 placed in the two sectors of the crucible.

2. Description of the system

2.1. Mechanical design

An existing 6 kW electron beam gun crucible is modified so that it could be rotated at different speeds during evaporation. A groove is made along the circumference of the crucible which can be partitioned into sectors depending on the number of evaporating materials. Figure 1 shows the new design of the crucible with two partitions in comparison with that of the conventional electron beam gun crucible. Different evaporating materials are then loaded in the sectors of the crucible. The deposition system is shown in Fig. 2. The crucible is rotated using a stepper motor (A) fixed outside the vacuum system. A Wilson seal (B) fixed to the base plate (C) of the evaporating unit is used as the rotating element for coupling the stepper motor and the electron beam gun crucible (D). The shaft of the Wilson seal is coupled to the electron beam gun through a chain
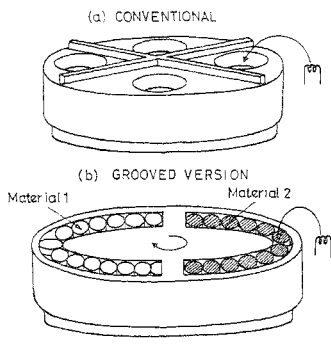

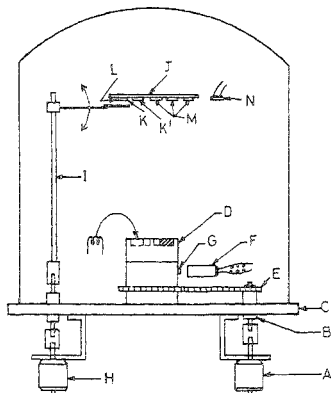FIG. 1. Electron beam gun crucible (a) conventional, and (b) grooved versions.

FIG. 2. Schematic view of the deposition system

and sprocket arrangement (E). A small nonmagnetic metal projection (G) is embedded in the circumference of the crucible. When this projection faces a position sensor (F) (proximity switch) positioned close to the crucible, the sensor gives a voltage output.

For evaporating two materials, the following procedure is used. The two materials with different vaporization temperatures were loaded into the two partitions of the crucible. When the initial position of the crucible is sensed, a set value of emission current and a specified speed of rotation are set for evaporating the first material in the crucible. These values are retained until the crucible crosses the first evaporating material. When the second evaporating material faces the electron beam, the emission current and speed will change automatically to the values set corresponding to the second material which depend on the vapour pressure of the material and the required rate of deposition. These values of current and speed are retained until the crucible crosses the second evaporating material. When the beam again faces the first material, the current and speed automatically get set to the values corresponding to the first material. This process repeats continuously until a required thickness is reached. The rate of deposition of the two materials is monitored using a home-made quartz crystal thickness monitor. An automatic shutter mechanism (I) has been used which enables the deposition of two materials separately on to two different substrates.

By controlling: (i) the speed of rotation; (ii) the electron beam emission currents, and (iii) the area of filling of each material in the grooved crucible, it is possible to get multicomponent films with required composition ratio. It is also possible to change the composition along the film thickness by continuously altering the speed and emission current during the film deposition.

2.2. Electronic design

The emission current and the speed of rotation of the crucible are controlled by making use of an INTEL 8085 microcomputer kit. The stepper motor is used for driving the crucible and an 8-bit DAC for controlling the emission current circuit which is housed on the electron beam gun control unit[1].

2.3. Performance evaluation

Two dielectric materials of high and low refractive indices have been chosen to obtain films with intermediate refractive indices (n) by controlling the composition of individual materials. The materials are cerium dioxide (n:2.0) and silicon dioxide (n:1.46) tablets. The films were deposited on to optically polished fused silica substrates, a silicon wafer and a copper substrate at a pressure of 1×10^{-6} mbar.

2.4. Preparation of homogeneous films

Mixed oxide films of CeO_2 and SiO_2 of different compositions[2] have been prepared by a proper choice of emission currents and speeds of rotation which in turn control the deposition rate of the two constituents. Atomic percentages of Ce, Si and O in the films have been calculated from weight per cent and compared with the data obtained from Auger, EDAX and RBS analysis. The results were found to be in good agreement. The refractive index of the mixed oxide films has also been calculated using the Lorentz–Lorenz formula. These values are compared with the refractive indices of the films as measured by ellipsometry and from the spectrophotometer. These results are in good agreement with theory.

2.5. *Preparation of graded index films*

Graded index films of CeO_2 and SiO_2 materials were prepared[3] by two methods, *i.e..*, (i) decrease in CeO_2 and increase of SiO_2 content from substrate–film to film–air interface along its depth, and (ii) increase in CeO_2 and decrease of SiO_2 content from substrate–film to film–air interface along its depth. Auger depth profile and RBS analysis revealed that the films were compositionally gradient along its thickness. Optical characteristics showed that films deposited at ambient and 300°C substrate temperatures were inhomogeneous in nature.

3. Conclusions

This technique has been found to be suitable to prepare homogeneous and graded mixed oxide films of required composition with tailored optical properties and structure. As a single electron beam source is used, it is much simpler, less expensive and uses less number of controls than the multisource deposition systems.

This technique can also be used for evaporating more than two materials (by increasing the number of sectors in the crucible) and also for specific applications such as preparation of alloys, cermets, etc.

References

1 SHIVALINGAPPA, L., NARASIMHA RAO, K.   Rotating crucible electron beam evaporation technique for
   AND MOHAN, S.   multicomponent films, *Vacuum*, 1993, **44**, 1031.

2. SHIVALINGAPPA, L., NARASIMHA RAO, K   Optical properties of CeO_2 and SiO_2 mixed oxide films,
   AND MOHAN, S.   *25th Boulder Damage Symp.*, NIST, Colorado, USA, October
                                            27–29, 1993.

3. SHIVALINGAPPA, L., NARASIMHA RAO, K.,   A novel deposition technique for the deposition of graded
   AND MOHAN, S.   mixed oxide films, *Natn. Symp. on Vacuum Sci and Technol.*,
                                            NPL, New Delhi, October 6–8,1993.

Thesis Abstract (M. Sc. (Engng))
Analysis of transmission lines with nonlinear source and loads by P. Sampath Napoleon
Research supervisors: M. Satyam and M. H. Kori (C-DOT)
Department: Electrical Communication Engineering

1. Introduction

Transmission delays in high-speed systems is an important parameter that decides the overall system performance[1]. The problem becomes more acute when the transmission line cannot be terminated with a matched load. Further, each transmission line feeds a number of loads at different points through its length. This situation is likely to result in malfunctioning of the system if proper design of the transmission line and termination are not carried out keeping in view the limitations of various subsystems. So far, the Bergeron method is used for the analysis of the transmission line with a single nonlinear termination and a nonlinear source[2, 3]. This is a graphical technique and involves considerable effort in obtaining the waveform at source and load ends. There is a provision in SPICE (simulation program with integrated circuit emphasis) for the simulator to analyse a transmission line loaded at different points through its length with linear

loads[4,5]. There is no readymade method in the published literature for analysing the transmission line performance when the transmission line is loaded with nonlinear loads at different points on its length. An attempt has been made by the author to model the nonlinear terminations as equivalent voltage-dependent nonlinear current source which is acceptable to the SPICE program. Using this model transmission line with nonlinear sources and nonlinear loads have been analysed.

2. Program of work

A few transmission line interconnects based on PCB technology are fabricated with different values of Z_0 (characteristic impedance), t_{pd} (propagation delay per unit length), and with different terminations and the waveforms are recorded at various points on the transmission line. SPICE analysis is carried out using voltage-dependent current source model for the nonlinear source and loads for these cases, and is compared with waveforms obtained through measurements.

3. Results

The nonlinear driver and receiver characteristics are modeled from the results of V–I characteristics obtained through measurements. This has been achieved by representing nonlinear resistor as a voltage-dependent current source. The value of the current is expressed as a polynomial in the voltage across it.

The correctness of this methodology has been checked in the following way.

1. The waveforms obtained through this method are compared with those obtained through lattice diagram in the case of linear source and a linear load. The analysis is done for the following cases:

a. LOW to HIGH transition	when the line is open ended.
b. LOW to HIGH transition	when the line is terminated with $R_L = 2 Z_0$
c. HIGH to LOW transition	when the line is open ended.
d. HIGH to LOW transition	when the line is terminated with $R_L = 2 Z_0$, where R_L = termination load resistance.

The results are identical in all cases.

2. The waveforms obtained through this method are compared with those obtained through Bergeron Plot technique in the case of uniform lossless line with a single nonlinear source (effective) and single nonlinear load (effective). The analysis is done for the following cases:

a. LOW to HIGH transition	when the line is terminated with $R_L = 4 Z_0$
b. LOW to HIGH transition	when the line is terminated with $R_L = 2 Z_0$
c. HIGH to LOW transition	when the line is open ended.
d. HIGH to LOW transition	when the line is terminated with $R_L = 2Z_0$.

It is found that the results from Bergeron Plots are close to the results from SPICE analysis, considering the errors due to inaccuracies involved in numerical and manual techniques of drawing Bergeron Plots.

3. Since no analytical check technique is available for the case of transmission lines with multiple impedance boundaries or discontinuities, nonlinear source, and multiple loads, it was decided to verify the validity of this by fabricating a PCB transmission line and measuring the waveform at different nodes and with different termination conditions.

The waveforms obtained through the proposed method are compared with those obtained through measurements on the experimental setup. The experimental setup was made with a PCB with known h (height over the ground plane), w (width of the microstrip trace), t (thickness), e_r (dielectric constant of glass epoxy), Z_0 (characteristic impedance), t_{pd} (propagation delay per unit length), and l (length of the trace). The load points were first loaded with 4.7 pf capacitors (the line had 8 load points at uniform intervals of 3 cm). The far end was either unterminated or with Thevenin termination or with Schotkky diode terminations. Results for the following cases are presented.

For LOW to HIGH transition

Case 1

When the load points were loaded with 4.7 pf capacitors and far end terminated with 220 ohms pull-down termination.

Case 2

When the load points were loaded with 4.7 pf capacitors and far end terminated with 100 ohms pull-down termination.

For HIGH to LOW transition

Case 3

When the load points were loaded with 4.7 pf capacitors and far end terminated with 100 ohms pull-down termination.

Case 4

When the load points were loaded with 4.7 pf capacitors and far end unterminated.

Case 5

When the load points were loaded with F244 (an octal buffer integrated circuit using Fairchild advanced Schottky transistor technology commonly used for driving receiving digital signals) and far end unterminated.

Case 6

When the load points were loaded with F244 and far end terminated with 100 ohms pull-down termination.

It has been found that the measured waveforms are in good agreement with the predicted waveforms. Possible reasons for the deviations are: (1) finite switching time of the clamping diodes provided at both input and output stages, (ii) circuit parasitics and their variation with voltage, (iii) waveform behaviour during the rise and fall time is not modeled, (iv) device characteristics variation due to power supply variations, (v) measurement process introduced errors like limited bandwidth, probe parasitics, and (vi) other electromagnetic interferences.

4. Conclusions

The study attempts to develop a methodology to calculate or analyse the waveforms on transmission lines terminated by nonlinear terminations at multiple points, using the SPICE program. This has been achieved by representing nonlinear resistor as a voltage-dependent current source. The value of the current is expressed as a polynomial in the voltage across it. The correctness of this methodology has been checked by comparing the waveforms obtained through this method with experimentally measured waveforms in the case of lossless transmission line with multiple impedance discontinuities, nonlinear loads and nonlinear source. It has been found that the measured waveforms are in good agreement with the predicted waveforms.

References

1. BLOOD, W. R. JR   *MECL system design handbook*, Fourth edn, 1983.

2. SINGLETON, R. S.   No need to juggle equations to find reflection---just draw three
                            lines, *Electronics*, 1968, 41, 93–99

3. STEHLIN, R. A.   Bergeron Plots predict delays in high-speed TTL circuits,
                            EDN, 1984, 41, 293–298.

4. TUINENGA, P. W.   *SPICE–A guide to circuit simulation and analysis using
                            PSPICE*, 1988, Prentice Hall.

5. THORPE, T. W.   *Computerized circuit analysis with SPICE A complete guide
                            to SPICE with applications*, 1992, Wiley.

Thesis Abstract (M.Sc. (Engng))
An approach to evaluation and selection of R&D projects for new products by
Dilip K. Das
Research supervisors: B. G. Raghavendra and B. K. Chandrasekar (Organisation)
Department: Management Studies

1. Introduction

Evaluation and selection of R&D projects become necessary when the total resources required by the R&D project proposals exceed the available resources of funds, manpower and facilities in an organisation. A properly framed evaluation method also helps in minimising the risks of technical and/or commercial failure of an R&D project. A poor evaluation system may give rise to Type-I or Type-II errors through the selection of potentially bad projects or the rejection of potentially good ones. These risks, along with the resources at stake, make the evaluation and selection process an important aspect of R&D management.

Considerable efforts have been made in recent years for the formulation of appropriate methods and models for evaluation and selection of R&D projects. These can be grouped into the following three categories, based on the techniques adopted:

(i) Comparative judgement methods, such as scoring, ranking[1,2].

(ii) Quantitative analysis methods involving operations research management science techniques[3–6].

(iii) Financial analysis methods, such as cost–benefit ratio, payback period, profitability index, etc.[7,8]

Comparative judgement methods are best suited for evaluation by peer groups or committees. A well-structured scoring format can capture the subjective assessments and preferences of the evaluators. But the available comparative judgement methods do not consider allocation of weights among the different evaluation criteria, as they are generally ad hoc in nature. Quantitative methods are found to be quite complex and require quantified inputs which may not be available at the evaluation stage. Quantitative models are also criticised for their inflexibility which make them unsuitable for different types of organisations and changed business environments. Financial analysis methods consider only the financial parameters, ignoring other vital aspects like resource constraints, technological features of the project, organisational capabilities and

such other factors. The need for a new approach emanates from the above-listed shortcomings of the existing methods. The approach proposed in this thesis attempts to incorporate the best of both the subjective assessments and the objective methods of quantitative analyses.

2. A project scoring method

The proposed approach adopts a weighted scoring-cum-financial analysis method for the evaluation of new-product R&D projects. The evaluation process is divided into the following three phases:

(i) a financial analysis phase;
(ii) a criteria scoring phase; and
(iii) a criteria weight determination phase.

2.1. *Financial analysis phase*

In this phase, a discounted benefit–cost ratio, called the financial index (FI) of the R&D project, is determined. The FI is given by

$$FI = \frac{\text{Net present value of the benefits of the project}}{\text{Net present value of the R\&D costs of the project}}.$$

The financial analysis phase involves the traditional cost–benefit ratio approach. The project life span may be used as the time span for discounting the benefits to the present values.

2.2. *The criteria scoring phase*

In this phase, a set of seven evaluation criteria are proposed for a new-product R&D project. These seven criteria are arranged in a structured format, amenable for scoring on a preset scale. Each criterion is further subdivided into four subcriteria, to add clarity and facilitate development of proper scores. An evaluator could compare different parameters of the R&D project being evaluated with each one of the criterion and the subcriterion and assign a score on the preset scale.

The criteria to be used for evaluation of R&D projects are related to the core competence and comparative advantages of an organisation. A SWOT (strengths, weaknesses, opportunities and threats) analysis, which is often advocated by strategic planners, is employed here for eliciting the following evaluation criteria for new-product R&D projects:

(i) Organisational capabilities with respect to R&D;
(ii) Organisational capabilities with respect to production;
(iii) Organisational capabilities with respect to marketing;
(iv) Demand for the product;
(v) Uniqueness and other special features of the product;
(vi) Technological complexity and other features of the R&D project; and
(vii) National and societal importance of the R&D project.

These seven criteria may have varying degrees of importance among different R&D projects and also across different organisations. Hence, appropriate weightages are to be assigned to each of these criterion, which could be determined using the method explained in the 'criteria weight-determination phase'.

2.3. *The criteria weight-determination phase*

In this phase, relative weights of the evaluation criteria are determined with the help of pairwise comparisons, using the theories of analytic hierarchy process (AHP), introduced by Saaty[9].

The relative weight of each criterion is determined by taking each possible pair of criteria and comparing the importance of one criterion with the other. This is accomplished by developing a pairwise comparison matrix. The comparison is carried out on a 1 to 9 ratio scale, where 1 indicates equal importance and 9, the absolute or maximum importance of one criterion over the other. The pairwise comparison matrix so obtained has the properties of a positive reciprocal matrix, whose normalised principal eigenvector gives the relative weights of the evaluation criteria for a particular R&D project.

Since the pairwise comparison process is based on subjective judgement, because of the transitivity lack of preferences, judgemental inconsistencies could occur. The consistency of the pairwise comparison process can be evaluated by the consistency index (CI), which is defined by

$$CI = (\lambda_{max} - n)/(n-1),$$

where λ_{max} is the principal eigenvalue of the pairwise comparison matrix. A CI of less than 0.1 indicates an acceptable level of consistency[9].

The weighted score of the R&D project is determined after the criteria scores are assigned and the criteria weights are computed. Then the 'project score' (PS) is defined as

$$PS = \sum_{i=1}^{n} \frac{W_i S_i}{S_{max}} \times 100$$

where W_i is the weight of the ith criterion, S_i, the score obtained by the ith criterion (sum of the scores obtained by the sub-criteria under the ith criterion), n, the number of evaluation criteria; and S_{max}, the maximum possible score.

3. Determination of 'project index' (PI) and project selection

The PI of a new-product R&D project is defined as the product of the FI and the PS. It is obvious that R&D projects with higher PI would be more prospective. For some R&D projects, it may become difficult to estimate the benefits in financial terms, during the project evaluation stage itself. Therefore, it may not be possible to determine the FI and therefore the PI of the project. In such cases, the PS could be used in place of PI for evaluation and selection of the projects.

When an R&D project is evaluated by a committee or more than one evaluator, the arithmetic mean of the project scores should not be used for selecting projects. This is because the criteria scores and the criteria weights belong to two different scales. The geometric mean of the criteria weights and the arithmetic mean of the criteria scores obtained by the evaluators, for each criterion, will yield the true central tendency and a PS determined with these values could be used for the ultimate selection of projects. When this PS is used for selection of R&D projects, it is advisable that each organisation sets up an upper and lower limit of PS for acceptance and rejection.

4. Validation of the approach

Two experiments were designed to determine the effect of the changes in the measurement scales, on the relative ranking of the R&D projects. In these experiments, six scales, *viz.*, 1–3, 1–5, 1–9,

1–25, 1–50 and 1–100, were chosen arbitrarily. Each scale was divided into five equal intervals or levels and numerical values were assigned to each of these levels. In the first experiment, a pairwise comparison matrix was constructed with the qualitative expressions explaining each level. Then six pairwise matrices were generated using the numerical values in each level and the PS were computed. It was observed from this experiment that although the PS varied from scale to scale, the relative ranking of the projects remained unchanged. A similar experiment was carried out for variations in the criteria scoring scale and the same conclusions were arrived at.

The questionnaire used for evaluation and selection of new-product R&D projects described here was mailed to six organisations, with two each in the R&D of private manufacturing organisations, R&D of public manufacturing organisation and the government R&D laboratories, to test the applicability of the approach in these organisations. The results received have been presented in the thesis.

5. Conclusion

The approach developed in the thesis attempts to capture the subjective assessment of the evaluators in a comprehensive manner, through criteria scoring and criteria weight determination phases. The financial analysis phase captures the performance of the project in the form of a financial benefit–cost ratio, subsequently linking it with the PI of the evaluated project. The evaluation criteria proposed here can be modified to suit the requirements of various types of organisations. It is also possible to incorporate additional criteria or modify the given set of criteria, for evaluation of 'defensive' research or basic research projects.

References

1. DEAN, B. V. AND NISHRY, M. J.   Scoring and profitability models for evaluating and selecting engineering projects, *Op. Res.*, 1965, **13**, 550–569.

2. MOTTLEY, C. M. AND NEWTON, R. D.   The selection of project for industrial research, *Op. Res*, 1959, **7**, 740–751.

3. BARD, J. F., BALACHANDRA, R.   An interactive approach to R&D project selection and termination, AND KAUFMAN, P.   *IEEE Trans.*, 1988, **EM-35**, 139–146

4. COOPER, R. G.   An empirically derived new product project selection model, *IEEE Trans*, 1981, **EM-28**, 54–61

5. DEAN, B. V. AND SENGUPTA, S. S.   Research budgeting and project selection, *IRE Trans*, 1962, **EM-9**, 158–169.

6. SCHWARTZ, S. L AND VERTINSKY, I.   Multi-attribute investment decisions: A study of R&D project selection, *Mgmt Sci.*, 1977, **24**, 285–301.

7. DISHMAN, S   Selecting R&D projects for profit, *Chem Engng*, 1962, **69**, 87–90.

8. RINGUEST, J. L. AND GRAVES, S. B.   The linear R&D project selection problems: An alternative to net present value, *IEEE Trans.*, 1990, **37**, 143–146.

9. SATTY, T L   *The analytic hierarchy process*, 1980, McGraw-Hill.

Thesis Abstract (M.Sc. (Engng))
A diffusion approach to modelling the adoption of bivoltine silk technology by Sandya Rao
Research supervisor: B. G. Raghavendra
Department: Management Studies

1. Introduction

India is the second largest producer of silk in the world, next only to China, producing about 13000 t of mulberry raw silk annually. The country earned over Rs 440 crores in 1991 through silk exports alone. Despite this, the quality of Indian silk has not risen to international standards[1]. Hence, efforts are being made by the Government of India to promote bivoltine silk, a superior quality silk of international standards. Several projects such as the National Silkworm Seed Project (1981) and the National Sericulture Project (1989), with financial assistance from the World Bank, were launched to promote the production of high-quality silk. However, these efforts have not been totally successful. Bivoltine silk accounts for a mere 2% of the total raw silk production in India as of today.

The main objective of this study is to analyse the growth and spread of bivoltine silk technology in the various districts of Karnataka State using a mathematical model and to explain the parameters of the diffusion process using profitability variables.

2. The Diffusion model

Geometry and Logistic models have traditionally been used in Diffusion modelling[2]. In this study, we compare the two models in terms of their fit to the data. Further, an attempt is made to explain the varying rates of diffusion across the districts of Karnataka State as a function of the profitability variables such as yield and area under mulberry.

Assuming that the spread of bivoltine technology is mirrored in the growing production of bivoltine reeling cocoons, data pertaining to the monthly bivoltine cocoon production from 1986-1993 was collected for each of the 20 districts of Karnataka State. Nine of the 20 districts were chosen for analysis as bivoltine cocoon production in these districts accounts for more than 80% of the total production in the state. Cocoon production is highly seasonal and hence deseasonalised moving averages were used for further analysis.

Both the Gompertz and the Logistic models were fitted to the bivoltine cocoon production data for each of the nine districts selected, using the Marquardt's method of nonlinear estimation and the rates of diffusion were obtained[2,3]. The Cochrane–Orcutt procedure was used to eliminate serial correlation in the residuals. Regression analysis was carried out to analyse the relationship between the profitability variables and the varying rates of diffusion across the districts[4]. Two
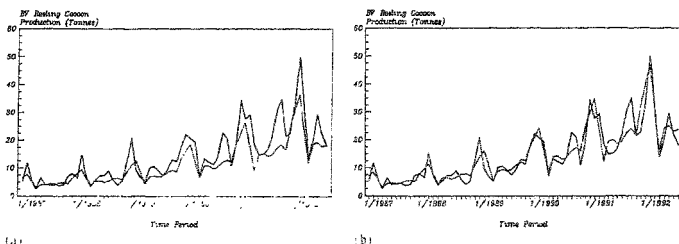

Fig. 1 Actual (—) and estimated bivoltine reeling cocoon production in Hassan District—(a) Logistic model, and (b) Gompertz model.

Table I
Comparison of the results of the Logistic and Gompertz models

Sl No	District	Logistic rate of difference	(R^2)	Gompertz rate of difference	(R^2)
1.	Bangalore	0.010	0.990	0.011	0.992
2.	Belgaum	0.005	0.993	0.004	0.993
3.	Chikmagalur	0.015	0.997	0.016	0.996
4.	Chitradurga	0.005	0.978	0.004	0.978
5.	D Kannada	0.025	0.998	0.033	0.997
6.	Hassan	0.017	0.998	0.016	0.998
7	Mandya	0.007	0.992	0.007	0.992
8	Mysore	0.015	0.996	0.017	0.996
9.	Tumkur	0.005	0.979	0.010	0.982

* after correction for serial correlation

profitability variables were selected for analysis, viz., bivoltine cocoon yield and the area under mulberry districtwise.

3. Results and discussion

It was found that both the models fit the data equally well. The actual and estimated values of the bivoltine reeling cocoon production obtained using the Logistic and Gompertz functions are shown in Fig 1. The rates of diffusion obtained from the two curves are remarkably similar after correction. The probable reason for both the curves giving such a good fit may be that the diffusion of bivoltine silk technology is still in its infancy and data pertaining to the entire range of the diffusion process is not available.

The analysis of the variations in the rates of diffusion across the various districts yielded conclusive results only for the yield variable. The area under mulberry in a district has negligible effect on the rate of diffusion of bivoltine silk technology in the district. The results suggest that efforts in the direction of improving yield would accelerate the rate of diffusion of bivoltine silk technology. This can be brought about by improving the extension programme, i e., educating the farmers on correct practices of mulberry cultivation and silkworm rearing and intensifying research efforts to develop disease-resistant, high-yielding varieties of bivoltine races.

The analysis taken up in this work throws light on the extent of adoption of bivoltine silk technology in the districts of Karnataka State and the factors responsible for the varying rates of diffusion across the districts. This work bridges the gap existing in literature in the area of diffusion modelling in sericulture.

References

1.   *Silk in India–Statistical biennial*, 1988, 1992, Central Silk Board, Bangalore.

2. MAHAJAN, V. AND PETERSON, R.   *Models for innovation diffusion*, 1985, Sage Publications.

3. MADDALA, G S.   *Econometrics*, 1986, McGraw-Hill

4 DRAPER, N R. AND SMITH, H   *Applied regression analysis*, 1981, Wiley

5 DIXON, R.   *Econometrica*, 1980, **48**, 1451–1461

Thesis Abstract (Ph. D.)
Studies on tRNAs and tRNA genes in cucumber (*Cucumis sativus*) chloroplasts by
Shailaja Hande
Research supervisor: C. Jayabaskaran
Department: Biochemistry

1. Introduction

Chloroplasts are semi-autonomous energy-transducing photosynthetically functional organelles found in plant cells. These organelles develop from precursors known as proplastids when exposed to light and to etioplasts when kept in dark. They contain their own DNA, RNA and all the machinery involved in replication, transcription and translation.

The objectives of the present investigation were: (i) to study the effect of light on chloroplast tRNA gene expression in cucumber *(Cucumis sativus)*, (ii) to purify and sequence a chloroplast tRNA[Pro] by post-labeling techniques to understand the unique secondary structural features, and (iii) cloning, sequencing and characterization of a tRNA[tRNA[Leu] (CAA)] gene and to study its organization and processing.

2. Experimental

Plastid tRNAs were prepared from cucumber cotyledons according to the procedure of Shinozaki and Sugiura[1]. Aminoacylation assays and 2D-PAGE were carried out according to the procedures of Burkard *et al.*[2,3] tRNA sequencing was done according to the method of Stanley and Vassilenko[4]. Studies on tRNA processing were carried out according to the method of Poll *et al.*[5]

3. Results and discussion

3.1. *Effect of light on tRNA gene expression*

Light is the coordinator of several events at different stages of leaf formation and the transformation of etioplasts to chloroplasts is one such developmental event that is mediated by light. The development of photosynthetically functional chloroplasts requires the coordinated expression of both nuclear and chloroplast genes since chloroplast proteins are coded by both nuclear and chloroplast genes. Recent developments have shown that light modulates the expression of nuclear genes coding for chloroplast proteins at the level of transcription, whereas it modulates the expression of chloroplast genes by post-transcriptional, translational and post-translational events. In order to examine the role of light in the modulation of chloroplast tRNA genes the following experiments were conducted.

To study and compare tRNA population in etioplasts and chloroplasts, ^{32}P-labeled total tRNA from the two sources was fractionated by two-dimensional polyacrylamide gel electrophoresis (2D-PAGE) and subjected to autoradiography.

Comparison of the autoradiograms revealed a similar pattern in both the plastid types except for the presence of nine extra tRNA species in etioplasts. These extra tRNA species could be due to the presence of tRNA with variation in their modified nucleotide content or due to the presence of new tRNA isoacceptors.

The relative levels of specific tRNAs in chloroplasts and etioplasts were determined by aminoacylation using *E. coli* aminoacyl synthetases and tritiated amino acid. The results obtained indicated that the levels of most of the tRNAs remained more or less equal in the two plastids. How-

ever, the amino acid acceptor activity of tRNA^{Lys}, tRNA^{Arg} and tRNA^{Tyr} (40, 44 and 50%, respectively) were dramatically reduced in etioplasts as compared to that in chloroplasts.

Northern analysis of specific chloroplast tRNAs, namely, tRNA^{Leu}(CAA), tRNA^{Leu}(UAG), tRNA^{Leu}(UAA), tRNA^{Phe}(GAA), tRNA^{Thr}(GGU), tRNA^{Glu}(UUC) and tRNA^{Tyr}(GUA) was carried out using gene-specific probes. The data obtained revealed that with the exception of tRNA^{Thr}(GGU), whose levels increased in etioplasts, the relative levels of most plastid tRNAs tested did not change appreciably in the two plastid types. However, aminoacylation data revealed reduced levels of functional tRNA^{Tyr} in etioplasts. This suggested that reduced aminoacylation of tRNA^{Tyr} could be due to defective tRNA^{Tyr} molecules (loss of 3'-CCA ends or undermodified tRNA^{Tyr}).

The extra tRNA species in the 2D-gels prompted us to investigate the isoacceptor profile of certain tRNAs as well as the degree of modification in total tRNA in etioplasts and chloroplasts. Light-induced alterations in the tRNA isoacceptor profile of tRNA^{Leu}, tRNA^{Phe}, tRNA^{Val} and tRNA^{Lys} in etioplasts and chloroplasts were examined by RPC-5 column chromatography of aminoacylated tRNAs. The results indicated that there were no changes in the number of isoacceptor species for these tRNAs. However, there were significant differences in the relative levels of two of the three tRNA^{Leu} isoacceptors and for both the isoacceptors of tRNA^{Val}. This indicated that although light did not cause the induction of new tRNA-isoaccepting species for the tRNAs tested, it modulated the expression of these tRNA genes.

Since modified nucleotide content of tRNA has an impact on the activity of tRNA, the effect of light on the modified nucleotide content of etioplast and chloroplast tRNAs was examined by the post-labeling technique. Modified nucleotides pi^{6}A/piO^{6}A, pψ, pm^{2}A, pGm, pm^2 G, pm^1 G, pTm, pT, pI, pD, pm^{5}C, pm^{7}G, pCm and pm^{1}A were identified in both total tRNA species. However, etioplast tRNAS were undermodified with respect to the modified nucleotides pi^6/piO^{6}A, pψ, pI, pGm, pm^{1}G, pT and pTm, while chloroplast tRNAs were undermodified with respect to pm^{1}A and pm^{2}A. Hence it is probable that the differences in the number of tRNA species that were observed in the 2D-gel pattern and the amino acid acceptor activity of tRNA in the two plastid types were due to the variations in the extent of tRNA modification. In conclusion, relative levels and/or amino acid acceptor activity of only some of the tRNA molecules studied were altered under conditions of etiolation. Since tRNAs play an important role in protein synthesis, limiting quantities of certain tRNA might have a regulatory role in protein synthesis. The results obtained suggested that transcriptional regulation occurs to a limited extent and that post-transcriptional events such as turnover, stability, modification and processing of tRNA probably play a major role in the control of tRNA gene expression in light-mediated changes brought about in chloroplasts.

3.2. *Structural features of tRNA^{Pro}*

In order to study the tRNA population in cucumber chloroplasts, total chloroplast tRNA (cold tRNA mixed with ^{32}P-labeled tRNA) was fractionated by 2D-PAGE into 37 species, out of which 20 tRNAs corresponding to 12 amino acids were identified by aminoacylation with *E. coli* aminoacyl–tRNA synthetases.

In order to study the structural aspects of chloroplast tRNA^{Pro} it was purified by RPC-5 column chromatography and 2D-PAGE. The sequence of this tRNA was determined by post-labeling technique. It was 77 nucleotides in length and had all the variant and semi-invariant features found in most tRNAs. It had the anticodon UGG. The most unusual feature of this tRNA was the absence of methylated GG residues at positions 18 and 19 in the dihydrouridine loop. It had the

modified nucleotides pD (position 20), pψ (positions 27, 38 and 55), pm^{7}G (position 46), pT (position 54), and an unknown modified A residue (position 37).

3.3. *Study of tRNA biosynthesis*

To study the organization, expression and biosynthesis of tRNA genes in cucumber chloroplast, a chloroplast genomic library was constructed using the vector pUC8 and the clones were screened with 3' end labeled chloroplast total tRNAs. Six positive clones were identified and one of the clones, pCL19, carrying a DNA segment of 1.7 kb, was isolated, subcloned and the sequence of the tRNA gene determined. The DNA segment contained tRNA^{Leu}(CAA) gene. The coding region of the gene was 81 bp long and showed 99% homology with the corresponding gene from spinach, broad bean, tobacco and maize, 98% homology with pea and 90% homology with livewort. The 5' flanking region of the gene contained two sets of −10-like (TATCAT and TAGAT) and −35-like (TTCCAT and TTGTCA) bacterial-promoter sequences. The 3' flanking region showed inverted repeats that could be transcription terminator signals.

Towards delineating the steps involved in the processing of the above tRNA gene, a 714 bp subfragment of clone pCL19 containing the gene was subcloned in the vector pSP64. ^{32}P-labeled precursor prepared from this subclone using SP6 RNA polymerase was incubated with pea chloroplast extract. In this study, mature tRNA was observed in all the experiments. It was shown that endonucleases were involved in the maturation of 5' and 3' ends of this tRNA. However, the simultaneous occurrence of the intermediates 5' leader + tRNA and 3' trailer + tRNA suggested that *in vitro* there was no specific order in the processing steps.

References

1. SHINOZAKI, K. Y. AND SUGIURA, M.   *Nucl. Acids Res.*, 1982, **10**, 4923.

2. BURKARD, G., GUILLEMAUT, P. AND WEIL, J. H.   *Biochem. Biophys. Acta*, 1970, **224**, 184.

3. BURKARD, G. *et al.*   In *Methods in chloroplasts molecular biology* (Edelman, M., Hallick, R. B. and Chua, N. H., eds), p. 347, 1982, Elsevier Biomedical Press.

4. STANLEY, J. AND VASSILENKO, S.   *Nature* (Lond.), 1978, **274**, 87.

5. POLL, A. M , HIBBERT, C. S., RADEBAUGH, C. A. AND HALLICK, R. B.   *Pl. Mol. Biol.*, 1988, **11**, 45.

Note